

Electric field reversals in the sheath region of capacitively coupled radio frequency discharges at different pressures

This article has been downloaded from IOPscience. Please scroll down to see the full text article.

2008 J. Phys. D: Appl. Phys. 41 105214

(http://iopscience.iop.org/0022-3727/41/10/105214)

The Table of Contents and more related content is available

Download details:

IP Address: 148.6.27.121

The article was downloaded on 13/08/2009 at 13:52

Please note that terms and conditions apply.

J. Phys. D: Appl. Phys. 41 (2008) 105214 (15pp)

Electric field reversals in the sheath region of capacitively coupled radio frequency discharges at different pressures

J Schulze¹, Z Donkó², B G Heil¹, D Luggenhölscher¹, T Mussenbrock³, R P Brinkmann³ and U Czarnetzki¹

- ¹ Institute for Plasma and Atomic Physics, Ruhr-University Bochum, Germany
- ² Research Institute for Solid State Physics and Optics of the Hungarian Academy of Science, Budapest, Hungary
- ³ Institute for Theoretical Electrical Engineering, Ruhr-University Bochum, Germany

E-mail: fjschulze@hotmail.com

Received 25 January 2008, in final form 26 March 2008 Published 1 May 2008
Online at stacks.iop.org/JPhysD/41/105214

Abstract

Electric field reversals in single and dual-frequency capacitively coupled radio frequency discharges are investigated in the collisionless (\leq 1 Pa) and the collisional (65 Pa) regimes. Phase resolved optical emission spectroscopy is used to measure the excitation of the neutral background gas caused by the field reversal during sheath collapse. The collisionless regime is investigated experimentally in asymmetric neon and hydrogen single frequency discharges operated at 13.56 MHz in a GEC reference cell. The collisional regime is investigated experimentally in a symmetric industrial dual-frequency discharge operated at 1.937 and 27.118 MHz. The resulting spatio-temporal excitation profiles are compared with the results of a fluid sheath model in the single frequency case and a particle-in-cell/Monte Carlo simulation in the dual-frequency case. The results show that field reversals occur in both regimes. An analytical model gives an insight into the mechanisms causing the reversal of the electric field. In the dual-frequency case a qualitative comparison between the electric fields resulting from the PIC simulation and from the analytical model is performed. The field reversal seems to be caused by different mechanisms in the respective regimes. In the collisionless case it is caused by electron inertia, whereas in the collisional regime it is caused by a combination of the low mobility of electrons due to collisions and electron inertia. Finally, the field reversal during the sheath collapse seems to be a general source for energy gain of electrons in both single and dual-frequency discharges.

1

(Some figures in this article are in colour only in the electronic version)

1. Introduction

Single and dual-frequency capacitively coupled radio frequency (CCRF) discharges are often used for industrial applications such as etching and deposition processes. For instance, these discharges are used as one of many steps in the production of integrated circuits [1]. In the bulk plasma the ion temperature is usually close to room temperature, whereas the electron temperature is a few electron volts. As the ion temperature is low, there is little uncontrolled damage of the substrate. By adjusting the sheath voltage,

the etching of microscopic structures by ion bombardment of the wafer surface can be controlled. In particular, dual-frequency CCRF discharges have become more important for industrial applications during the recent years. The advantage of these discharges is separate control of ion energy and ion flux impinging on the substrate surface [2–5]. However, recent investigations [6–9] have shown that this separate control is limited due to the coupling of both frequencies.

Despite this enormous relevance for applications, fundamental phenomena such as electron heating and electron dynamics particularly at low pressures and in dual-frequency

CCRF discharges are not yet fully understood and represent an important current research topic.

Within one RF cycle there are different mechanisms leading to an energy gain of electrons as a result of the plasma interacting with its boundary sheath in electropositive discharges:

- During the phase of sheath expansion electrons are accelerated from the sheath into the plasma bulk by the expanding sheath. In single frequency discharges this mechanism has been investigated both theoretically [10–16] and experimentally [17–24] at high and low pressures in different gases. In dual-frequency CCRF discharges electron heating by the expanding sheath has been observed experimentally [9] and theoretically [25]. However, in the case of dual-frequency CCRF discharges the number of investigations is limited and restricted to particular conditions.
- During the phase of maximum applied voltage and full sheath expansion secondary electrons can contribute considerably to ionization and, therefore, to plasma sustainment [1, 17, 21, 26, 27]. Secondary electrons are produced at the electrode surface by ion bombardment and are accelerated into the plasma bulk by the electric field in the sheath. The production of secondary electrons strongly depends on the discharge conditions. Ionization due to secondary electrons is most efficient at high pressures, high sheath voltages and electrode materials with high secondary electron emission coefficients.
- During the phase of sheath collapse electrons can gain energy by a local reversal of the electric field at the sheath edge under certain conditions. sheath collapses so fast that electrons cannot follow by diffusion, a locally reversed electric field builds up that accelerates electrons towards the electrode in order to support a constant current. In single frequency discharges at low pressures such field reversals were observed experimentally in argon by electron beam probe measurements [28] and theoretically in a PIC simulation of hydrogen discharges [29]. The occurrence of the field reversal is explained by electron inertia effects in both works. In single frequency discharges at high pressures, field reversals were observed experimentally in hydrogen [18,19,20,22] and theoretically in nitrogen [30], helium [27] and hydrogen [14, 19]. At high pressures, the field reversal is explained by a collisional drag force on the electrons, which prevents electrons from advancing into the sheath. In electronegative discharges double layers during the phase of sheath collapse were observed [17, 31, 32]. These double layers are closely related to the existence of negative ions in the discharge. Such phenomena in electronegative discharges are not discussed in this work.

A field reversal has been observed neither experimentally nor theoretically yet in dual-frequency CCRF discharges.

The focus of this paper is on the energy gain of electrons by local field reversals in single and dual-frequency discharges in both collisionless and collisional regimes. Applying phase resolved optical emission spectroscopy (PROES), spatiotemporal plots of the excitation into specifically chosen energy levels are obtained. One-dimensional spatial resolution along the discharge axis and temporal resolution within the RF period is achieved. Such plots show an energy gain of electrons during the sheath collapse. Measurements are performed in asymmetric single frequency hydrogen and neon discharges at 13.56 MHz at low pressures (\$1 Pa) and in a symmetric industrial dual-frequency discharge operated at 1.937 and 27.118 MHz in a He–O₂ gas mixture at higher pressure (65 Pa). The results are compared with those derived from a particlein-cell/Monte Carlo code (PIC/MCC) simulation of a dualfrequency discharge and a fluid sheath model of the single frequency discharge. An analytical model, which yields the electric field during the sheath collapse, is derived to describe the effect in both regimes and in single as well as dualfrequency discharges. This model is applied explicitly to the dual-frequency case using input parameters from the PIC simulation, which is performed under conditions similar to the ones investigated experimentally. The resulting electric fields are compared with those resulting from the PIC model quantitatively. Different terms contributing to the field reversal are identified with physical mechanisms using the analytical model. At low pressures, of typically 1 Pa or below, and in asymmetric discharges the current is no longer sinusoidal, but shows strong high frequency oscillations due to the excitation of the plasma series resonance (PSR) often referred to as the geometric resonance [23, 24, 33–35]. This non-sinusoidal RF current is measured in a single frequency discharge simultaneously to the PROES measurements which show the field reversal. This non-sinusoidal current is expected to have an effect on the field reversal.

The paper is structured in the following way. In section 2 the experimental setups of both the single and dual-frequency discharges are introduced and the applied diagnostics are explained. In section 3 a short description of the simulations is given. Section 4 presents the experimental and theoretical results. The discussion of the results and the analytical model to describe the field reversal in both regimes are presented in section 5. Finally, conclusions are drawn in section 6.

2. Experimental setup

2.1. Single frequency CCRF discharge

In the case of the collisionless regime, measurements are performed in a modified hybrid GEC reference cell [36]. The setup can principally be operated as a combination of ICP and CCP discharge (see figure 1). The metal cylinder surrounding the ICP antenna and the dielectric window are replaced by a monolithic quartz housing. Here the inductive coupling is not used. The RF voltage is applied only to the lower electrode and the whole chamber wall acts as the grounded electrode. Therefore, the discharge is strongly asymmetric and almost the entire voltage is dropped across the sheath at the powered electrode. The electrode and chamber walls are made of stainless steel. The electrode radius and gap between electrode and quartz are both 5 cm.

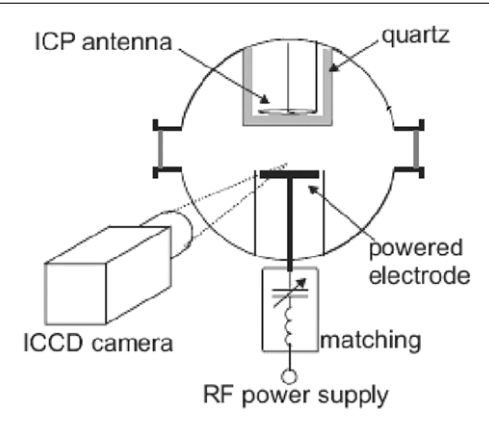


Figure 1. GEC reference cell and ICCD camera used for PROES in the case of an asymmetric single frequency CCRF discharge operated at 13.56 MHz.

PROES measurements are performed in molecular gas discharges, H₂, as well as rare gas discharges, neon, at low powers of 8 W and at pressures of 1 Pa or below. In the case of H_2 the plasma induced emission at Balmer- α , excitation energy 12.1 eV [37], is detected spatially and temporally resolved by an Andor iStar ICCD camera. In the case of neon emission from the Ne 2p₁ state, excitation energy 19 eV, is observed. The camera is synchronized with the RF-generator via a frequency divider and operated at the maximum repetition rate of the camera, 30 KHz. The lifetimes of the upper level of the H-Balmer- α line, 10 ns, and the Ne 2p₁ state, 14.5 ns [37], are short enough to resolve electron dynamics within one RF cycle at 13.56 MHz ($T_{RF} = 74 \,\text{ns}$). Figure 2 shows the principle of phase resolved measurements. The internal delay generator of the ICCD camera sets a certain delay between the trigger and the camera gate. Here the minimum camera gate width of 4.2 ns is used. Signal is acquired at a specific phase during several thousand RF cycles. Then the delay is increased and a different phase is scanned. Here a step width of 2.1 ns is chosen. 38 steps are performed, and a bit more than one RF cycle is scanned. Typical exposure times are 10 s for each step. All images are binned in the horizontal direction in order to reduce the noise resulting in one-dimensional spatial resolution along the discharge axis. We estimate the vertical spatial resolution to be 0.5 mm.

Neglecting cascade contributions and excitation out of metastable states, the excitation $E_i(t)$ can be determined from the measured emission [21]:

$$E_i(t) = \frac{1}{A_{ik}n_0} \left(\frac{\mathrm{d}n_{\mathrm{ph},i}(t)}{\mathrm{d}t} + A_i n_{\mathrm{ph},i}(t) \right). \tag{1}$$

Here A_{ik} is the transition probability of the observed emission, n_0 is the ground state density, $n_{\text{ph},i}(t)$ is the measured number of photons per unit volume and time and $A_i = (1/\tau)$ is the decay rate that is given by the inverse of the lifetime τ .

The RF voltage is measured simultaneously to the PROES measurements at the output of the matching box directly in front of the powered electrode using a LeCroy high voltage probe. The current to the chamber wall is also measured simultaneously by a Plasmetrex current sensor, which is integrated into the side wall of the GEC cell (figure 3).

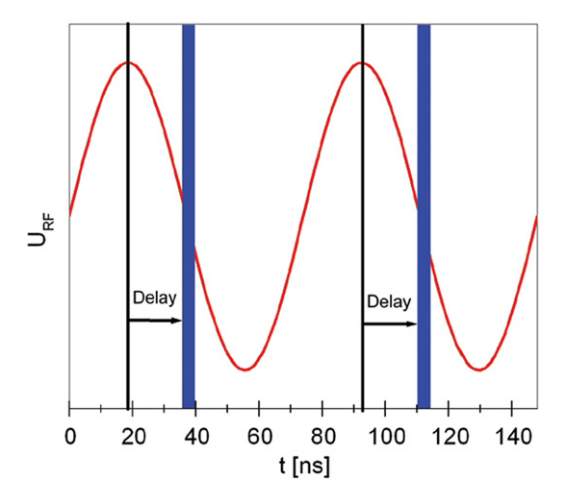


Figure 2. Principle of PROES measurements in a single frequency CCRF discharge.

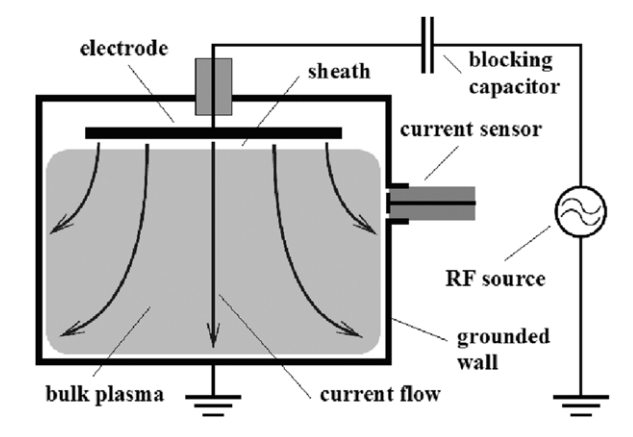


Figure 3. Sketch of the experimental setup including the diagnostic used for the measurements of the RF current waveform (current sensor) [35].

This sensor locally picks up a fraction of the RF current. This diagnostic—known as self-excited electron resonance spectroscopy (SEERS) [38, 39]—is used as a non-invasive process monitoring technique in the semiconductor industry.

2.2. Dual-frequency CCRF discharge

In the collisional regime PROES measurements are performed in a Lam Exelan process chamber, which is described in detail elsewhere [9]. It is a modified industrial dual-frequency CCRF discharge with plane parallel electrodes separated by a gap of 12 mm, see figure 4. Two RF voltages are applied simultaneously to the bottom electrode, whereas the top electrode is grounded. The electrodes are made of silicon with a radius of 110 mm. The plasma is confined in the radial direction by adjustable quartz rings, which shield it from the chamber walls. Thus, the discharge is almost symmetric.

For these experiments, the discharge is operated at $P_{\rm hf} = 800 \, \rm W$ and $P_{\rm lf} = 200 \, \rm W$ at $p = 65 \, \rm Pa$. The RF signals are fixed in frequency at 1.937 and 27.118 MHz with a common phase reference ($f_{\rm hf} = 14 \, f_{\rm lf}$). Measurements are performed in a 72% He–19% O_2 discharge with a 9% admixture of neon used as reference gas for PROES.

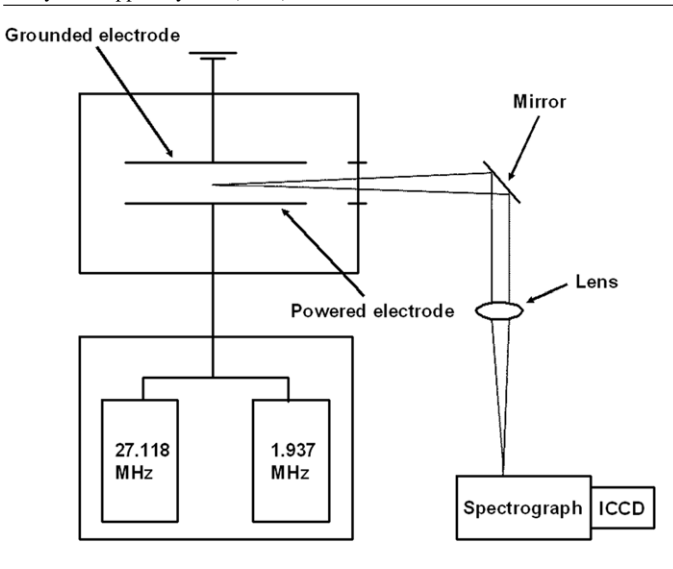


Figure 4. Experimental setup used for PROES measurements in a dual-frequency CCRF discharge.

The plasma emission is focused on the entrance slit of a Carl Zeiss PGS 2 spectrometer (300–900 nm) by a lens. In the spectrograph the light is dispersed and then detected by a fast gateable ICCD camera (PicoStar HR, LaVision), which is triggered by and synchronized with the low frequency RF signal. The temporal gate width used for phase resolved measurements in the dual-frequency case is 4.1 ns. This gate width yields a temporal resolution well within the high frequency RF cycle.

3. Simulations

3.1. Fluid sheath model for the single frequency case

In order to calculate the electric fields in single frequency CCRF discharges, a fluid sheath model is used [40,41]. Space-and time-resolved electric fields are calculated within one RF cycle in a symmetric argon discharge operated at 13.56 MHz at 10 Pa. This model assumes that the driving RF frequency is much higher than the ion plasma frequency and much lower than the electron plasma frequency. This is equivalent to assuming that the ions only react to the time averaged electric field. Further, electromagnetic effects are assumed to be negligible [42] and, thus, the electrostatic approximation is used for calculating the time dependent electric field.

The space- and time-resolved electric field E(x, t) is calculated using the following equation, which is derived by a matched asymptotic expansion about the point s [41], defined by equation (3):

$$E(x,t) = \begin{cases} -\frac{e}{\epsilon_0} \int_x^s n_i(x') \, dx' & x < s(t), \\ -\frac{kT_e}{en_i(x)} \frac{\partial n_i}{\partial x} & x > s(t), \end{cases}$$
$$-\frac{kT_e}{e} \frac{1}{\overline{\lambda}_D} \Delta \Psi_0' \left(\frac{x - s(t)}{\overline{\lambda}_D} \right) - \frac{kT_e}{e\overline{n}_i} \frac{\partial \overline{n}_i}{\partial s} \Delta \Psi_1'$$
$$\times \left(\frac{x - s(t)}{\overline{\lambda}_D} \right)$$
(2)

with

$$\int_{-\infty}^{s} n_{e}(x) dx = \int_{s}^{\infty} (n_{i} - n_{e}) dx, \qquad (3)$$

where $\overline{\lambda}_D = \sqrt{(\varepsilon_0 T_{\rm e}/e^2 \overline{n_{\rm i}})}$ and $\overline{n_{\rm i}}$ are the Debye length and ion density at the point s, respectively. k is the Boltzmann constant $T_{\rm e}$ is the electron temperature, $n_{\rm e}$ is the electron density and $n_{\rm i}$ is the ion density. Instead of treating the sheath as having a hard electron edge or wall, equation (2) approximates a realistic electron density and calculates a realistic electric field in the sheath. The functions $\Delta\Psi_0'$ and $\Delta\Psi_1'$ transition the electric field calculation smoothly from the electron depletion region dominated by ions to the quasineutral where the field is an ambipolar field.

Equation (2) is used in conjunction with an equivalent circuit model to iteratively calculate the time dependent electric field in the sheath. An ion model yields the ion density. To make this equation solvable the equation is transformed from being a function of position and time into being a function of the 'charge coordinate' and the time dependent charge across the sheath. The idea behind this is that the ion density is assumed to be monotonically increasing, and the integral of the ion density then replaces the spatial coordinate. When s is transformed into charge coordinates, it is equivalent to the charge across the sheath, Q(t). The point of this is that s is an unknown quantity, but if the rf current is known then Q(t) can be determined.

The transformed equation is then used with an equivalent circuit model of the plasma. The equivalent circuit model supplies the sheath model with Q(t), and the sheath model supplies the equivalent circuit model with the non-linear charge voltage relationship of the sheath. The two are used in an iterative scheme that calculates the Fourier components of the RF current in the discharge and the time dependent electric field in the sheath. This will be described in more detail in upcoming publications. This model has been tested successfully against space- and time-resolved measurements of the electric field in the sheath of an asymmetric CCRF discharge [23, 24].

The resulting ambipolar field during the phase of sheath collapse is compared with the electric field in a dual-frequency discharge at similar phases resulting from a PIC/Monte Carlo simulation, see below, and to an analytical model.

3.2. Simulation model for the dual-frequency case

The dual-frequency discharges studied here are described by a one-dimensional (1d3v) bounded plasma particle-in-cell model, complemented with Monte Carlo treatment of collision processes (PIC/MCC). The electrodes are assumed to be infinite, planar and parallel. As in the experiments the diameter of the electrodes was much larger than the electrode separation ($D/L \cong 18$), and as successful efforts have been made to improve the symmetry of the discharge, the 1D simulation is expected to capture all basic physical phenomena of interest. In our implementation of the PIC simulation, one of the electrodes is driven by a voltage

$$V(t) = V_{\rm hf} \sin(2\pi f_{\rm hf}t) + V_{\rm lf} \sin(2\pi f_{\rm lf}t), \tag{4}$$

while the other electrode is grounded [43]. The two excitation voltages are locked in phase, as was done in the experiments.

The simulations are carried out both for helium and argon gases. The collision processes considered for electrons are elastic scattering, excitation of background gas atoms to several energy levels, as well as ionization. The cross sections for these processes have been taken from [44] and [45], respectively, for He and Ar. For the positive ions—following the recommendation by Phelps—elastic collisions with the gas atoms have been divided into an isotropic and a backward part [46]. The cross sections for these collisions have been taken from [46, 47].

The number of superparticles in the simulations is typically 10⁵, which is expected to provide acceptable accuracy, although in the case of argon slight dependence of the results on the number of superparticles has been observed even in this range [48]. Our studies show that simulations of He discharges (He shows no Ramsauer effect) are less susceptible to this problem.

In contrast to most studies, in our case the electrodes reflect the electrons arriving at their surface with a pre-defined probability, usually taken to be 0.2. Additionally, we consider the emission of secondary electrons from the electrodes. Their important role in dual-frequency discharges has recently been studied by Turner [49]. Typical secondary yields used in this work range between 0.1 and 0.45, which are reasonable for Si electrodes [50].

The simulations provide the spatio-temporal distributions of several discharge characteristics. The distribution of the electron impact excitation is in direct correspondence with the light intensity distributions observed by PROES. Other quantities, such as space- and time-resolved electric field, particle velocities, and currents, aid the interpretation of the experimental data and the understanding of the discharge physics.

4. Results

In the following section, we present experimental as well as theoretical results for single and dual-frequency CCRF discharges: first, experimentally obtained spatio-temporal plots of the excitation into specifically chosen energy states in single and dual-frequency discharges are shown. Further, spatio-temporal plots of the electric field in the dual-frequency discharge resulting from the PIC simulation under conditions similar to the experiment are presented. Finally, the space-and time-resolved electric field resulting from a fluid sheath model in the single frequency case is shown. A more detailed analysis of these results is performed in section 5.

Figure 5 shows a spatio-temporal plot of the excitation into Ne 2p₁ in a single frequency rare gas, neon, discharge operated at 30 Pa, 8 W and 13.56 MHz within one RF period (74 ns). At such a high pressure only excitation caused by the expanding sheath is observed [17–23]. A beam of highly energetic electrons is generated by the expanding sheath, which penetrates into the plasma bulk. This beam is damped fast by collisions with the background gas at 30 Pa. Therefore, only excitation close to the sheath edge is observed. Here the sheath

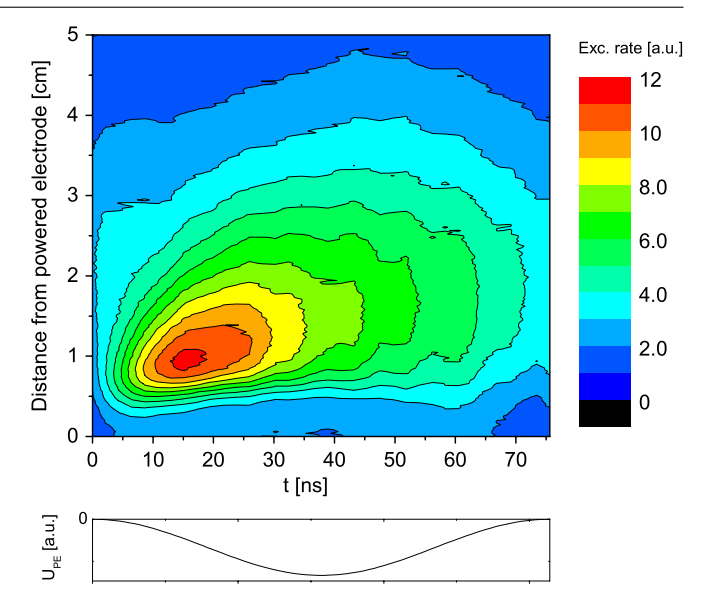


Figure 5. (Top graph) Phase and space resolved excitation into Ne 2p₁ in a single frequency neon discharge operated at 30 Pa, 8 W and 13.56 MHz. (Bottom graph) Sketch of the RF potential at the powered electrode.

edge is defined as the position where the excitation starts to increase significantly, 0.8 cm in figure 5 at 15 ns.

Figure 6 shows spatio-temporal plots of the excitation into Ne 2p₁ at lower pressures of 1 Pa (left graph) and 0.5 Pa (right graph) within one RF cycle. At the beginning of the RF period, the generation of a beam of highly energetic electrons by the expanding sheath is clearly observed in both cases [23]. In such spatio-temporal plots of the excitation an electron beam appears as a tilted trajectory and is indicated in the figures by arrows. At these low pressures the sheath width is much bigger (2.5 cm at 40 ns) and the RF current is not sinusoidal [24, 33, 34]. Consequently, the sheath expansion velocity is much higher. This enhances the generation of an electron beam, which propagates through the entire bulk until it hits the opposing quartz cylinder. The quartz acts as a floating surface in the plasma and charges up negatively. As a consequence of this a sheath builds up in front of the quartz, which reflects beam electrons which arrive at the quartz at a later time, back into the bulk. The trajectory of the reflected beam is clearly visible at 0.5 Pa. Under the conditions investigated here the plasma is heated effectively, since the beam is reflected and its energy is deposited in the plasma to a great extent. If the opposing surface was grounded instead of floating, the beam would still be reflected, since the floating potential would be the same. In both cases (grounded or floating surface) electron and ion fluxes must balance at the surface within one RF period. The only difference between a grounded and floating surface is that the particle fluxes must balance locally in the case of a floating surface and globally in the case of a grounded surface. However, this difference only plays a role in magnetized plasmas, where it can lead to strong electric fields in the plasma.

In contrast to higher pressures, at 1 Pa and 0.5 Pa an additional source of excitation is observed during the sheath collapse. Similar to the trajectory of the electron beam

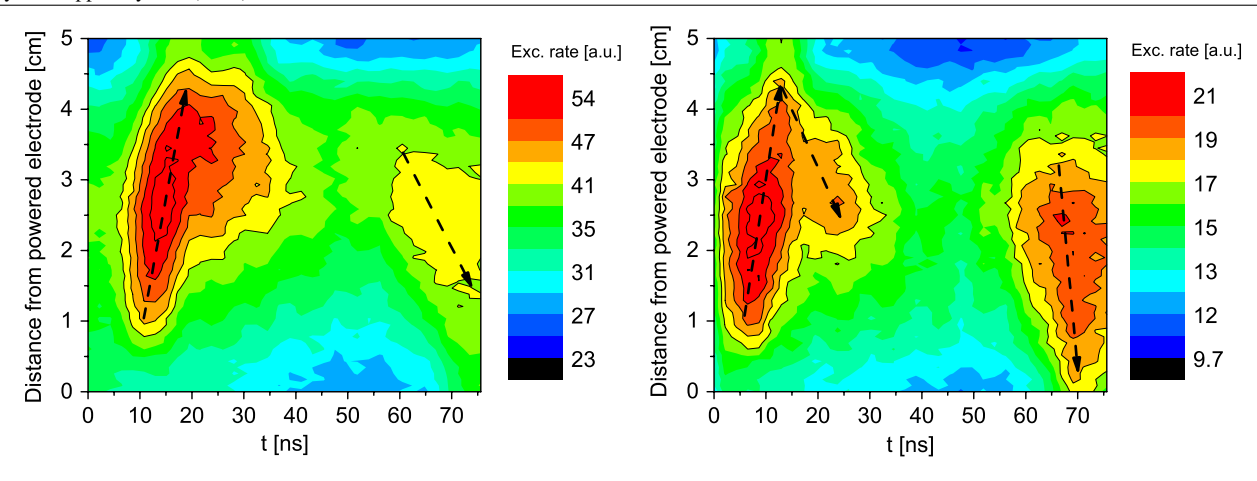


Figure 6. Phase and space resolved excitation into Ne 2p₁ in a single frequency neon discharge operated at 1 Pa (left graph) and 0.5 Pa (right graph). In both cases the discharge is operated at 8 W and 13.56 MHz.

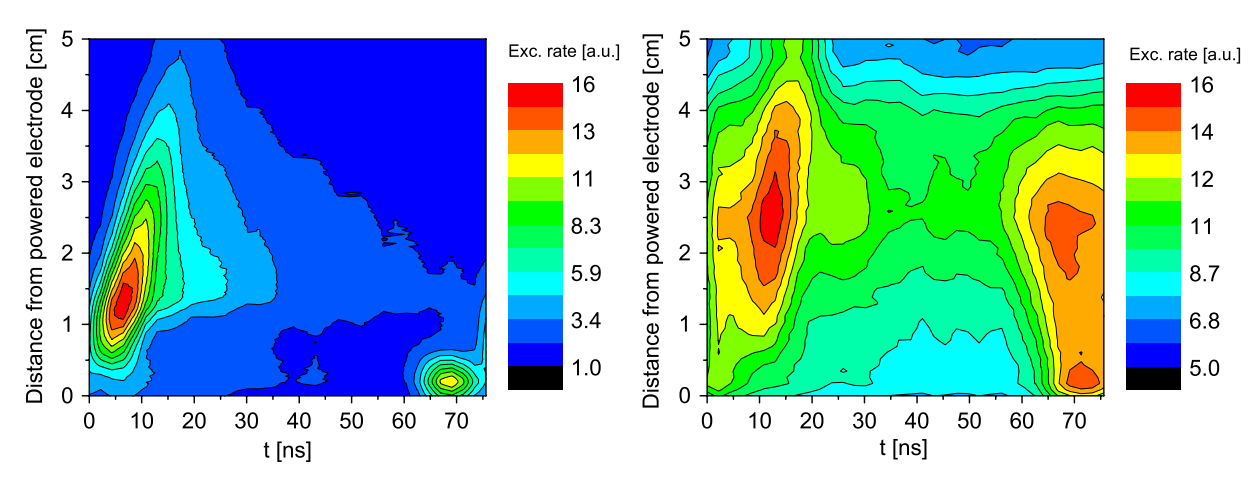


Figure 7. Phase and space resolved excitation into the n=3 state of atomic hydrogen (Balmer- α emission) in a single frequency H₂ discharge operated at 10 Pa (left graph) and 0.5 Pa (right graph). In both cases the discharge is operated at 8 W and 13.56 MHz.

generated by the expanding sheath, the excitation structure during the sheath collapse is also tilted. However, it is tilted in the opposite direction, indicating an acceleration of electrons towards the electrode. Sato and Lieberman measured a reversed electric field at the sheath edge during the phase of sheath collapse at similar pressure (0.3 Pa) in argon [28]. In this work this double layer disappeared with increasing pressure. According to their results we assume the observed excitation during the phase of sheath collapse to be caused by a local field reversal at the sheath edge. Similar to their investigations, the effect vanishes with increasing pressure. A detailed discussion of the cause of this field reversal is presented in section 5.

Figure 7 shows spatio-temporal plots of the excitation into the n=3 state of atomic hydrogen (Balmer- α emission) in a single frequency H_2 discharge operated at 8 W and 13.56 MHz at different pressures of 10 Pa and 0.5 Pa. At 10 Pa an excitation maximum close to the electrode during the phase of sheath collapse is observed. At 0.5 Pa two excitation maxima during the phase of retreating sheath are observed, one close to the electrode and one further inside the plasma at an earlier phase.

The spatio-temporal evolution of the electric field and the excitation into the n=3 state of atomic hydrogen (Balmer- α emission) in the sheath of a H₂ CCRF discharge at 80 Pa were measured before [20]. In this work an excitation

maximum close to the electrode during the phase of sheath collapse was observed, which could directly be identified with a field reversal. However, these measurements were performed at much higher pressures, where the regime is collisional, whereas it can be assumed to be collisionless at 0.5 Pa.

Vender and Boswell explicitly predicted two different field reversal mechanisms, which lead to an increased electron loss to ensure current continuity. According to their simulation [29], a field reversal at the electrode surface occurs if the wall potential rises and the plasma potential lags behind. They also mention a second mechanism leading to a field reversal close to the sheath edge during sheath collapse: if the sheath collapses so fast that electrons cannot follow and compensate the ion space charge, the changing wall potential drives a field reversal within the ion sheath. Obviously, both mechanisms are observed experimentally here (figure 7).

The left plot in figure 8 shows a spatio-temporal plot of the experimentally determined excitation into Ne $2p_1$ in a symmetric, industrial, dual-frequency CCRF discharge (Lam Exelan) operated at 65 Pa in He–O₂ with small neon admixture [9]. The exact conditions are mentioned in section 2.2. The spatio-temporal excitation profile is complex and depends on the coupling of both frequencies as described in [9]. The relative phase of the RF potential at the

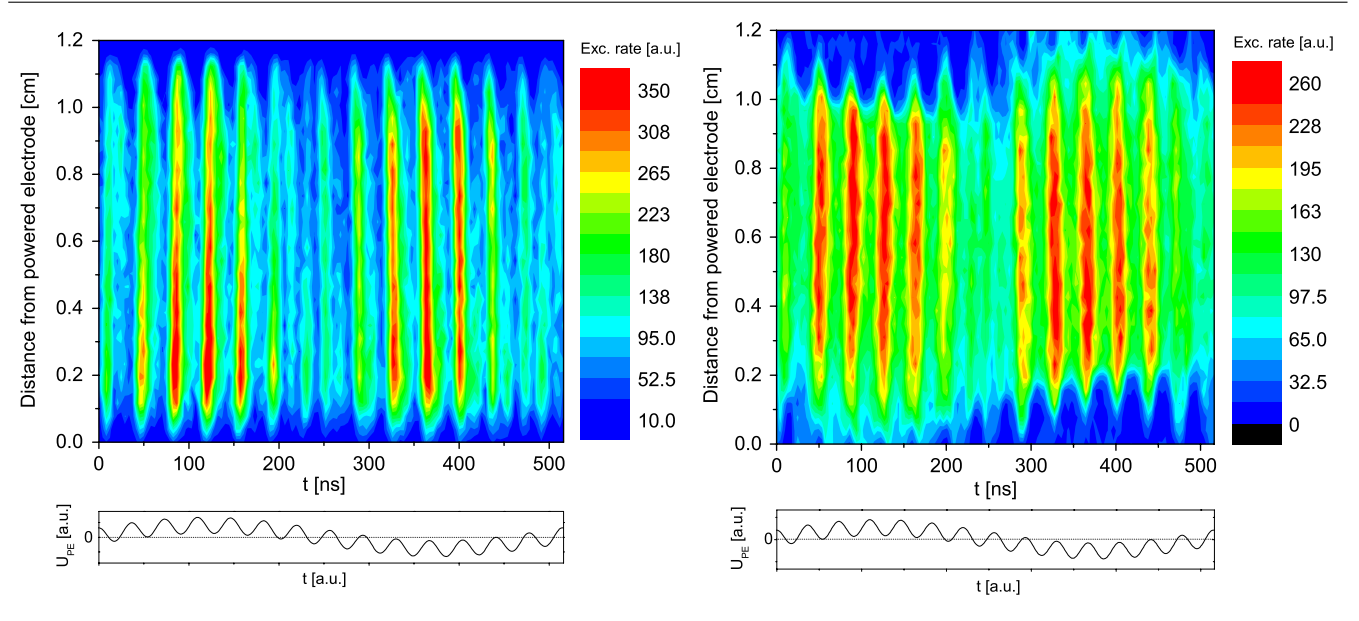


Figure 8. (Left) Experimentally determined phase and space resolved electron impact excitation function into Ne $2p_1$ in the Exelan at 65 Pa and sketch of the RF potential at the powered bottom electrode. (Right) Phase and space resolved excitation as it results from a PIC simulation (He, 65 Pa).

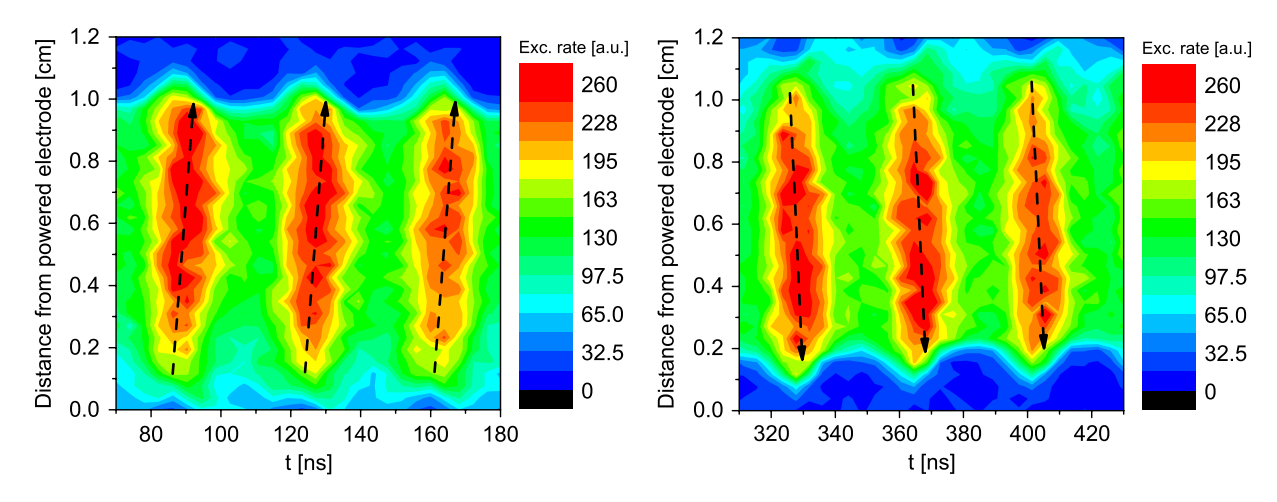


Figure 9. Spatio-temporal excitation within the first and second half of one low frequency RF period as it results from the PIC simulation.

bottom electrode is also shown qualitatively. Each excitation maximum corresponds to the trajectory of an electron beam generated by the expanding sheath.

In order to investigate field reversals in dual-frequency CCRF discharges a PIC simulation is performed, which yields access to a variety of plasma parameters with high spatial and temporal resolution. For simplicity, helium has been chosen as a model gas, since it is the main constituent of the experimentally used gas mixture. The applied frequencies and discharge geometry are identical to the experimental conditions. The applied low and high frequency voltages are $V_{\rm lf} = 800 \, \rm V$ and $V_{\rm hf} = 550 \, \rm V$, respectively. A gas pressure of 65 Pa (same as in the experiment), a gas temperature of 400 K, a secondary electron emission coefficient of $\gamma = 0.45$ [50] and an electron reflection coefficient of $\alpha = 0.2$ are used as input parameters. The right plot in figure 8 shows the total spatio-temporal excitation as it results from the PIC simulation. Good agreement between experiment and simulation is found supporting the validity of the simulation.

Figure 9 shows the spatio-temporal excitation as it results from the simulation during fractions of the first and second half of one low frequency RF period, respectively (zoom into figure 8). Obviously, the excitation maxima are tilted. They are tilted to the right during the first half of one lf RF period and to the left during the second half. Similar tilts are observed experimentally and are discussed in more detail in a forthcoming publication. In analogy to the results of PIC simulations in single frequency CCRF discharges performed by Vender [15] and Wood [16] and experimental investigations using PROES [23, 24], we identify these tilted excitation maxima with paths of beams of highly energetic directed electrons. Obviously, electron beams are generated at the bottom electrode during the first half and at the top electrode during the second half. From the tilt of the arrows in figure 9 the propagation velocity of these beams can be estimated to be about $2 \times 10^6 \,\mathrm{m\,s^{-1}}$.

Figure 10 shows sections of figure 8 directly in front of the powered bottom electrode during the first half of one low

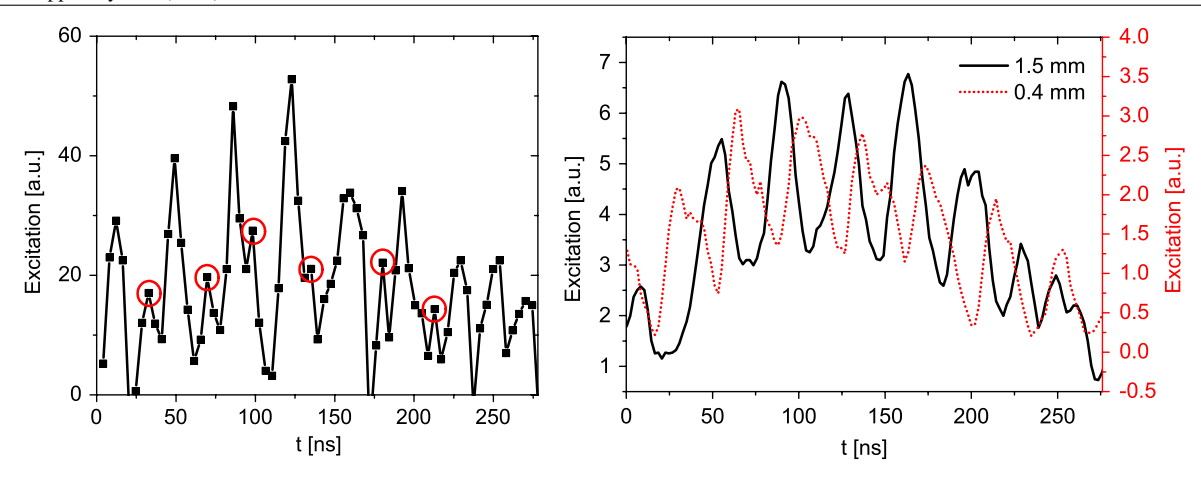


Figure 10. (Left) Experimentally determined excitation into Ne $2p_1$ at a distance of 0.4 mm in front of the bottom powered electrode during the first half of one low frequency RF cycle. The circles indicate excitation caused by a localized field reversal [51]. (Right) Spatio-temporal excitation at two different positions close to the powered electrode as it results from the PIC simulation.

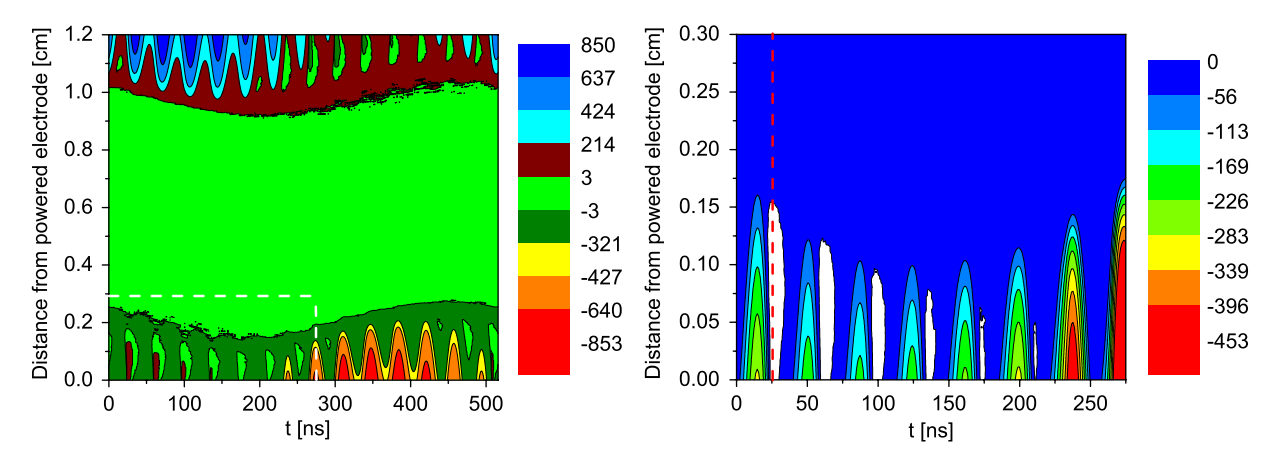


Figure 11. (Left) Phase and space resolved electric field in a dual-frequency helium discharge operated at 65 Pa as it results from a PIC simulation. The electric field is given in units of kV m⁻¹. (Right) Zoom into the left graph within the area indicated by the white rectangle.

frequency RF cycle under the same conditions as before [51]. The left plot in figure 10 shows the experimentally determined excitation 0.4 mm in front of the bottom electrode. The main maxima correspond to the beam trajectories shown in figures 8 and 9. However, in this profile more detailed structures are observed. Between two major excitation maxima, which occur at the phases of high frequency sheath expansion, additional maxima are detected. These weaker maxima occur at distinct phases of high frequency sheath collapse. The PIC simulation yields similar results. The right plot in figure 10 shows the excitation as it results from the simulation at two positions in front of the bottom electrode. At 0.4 mm only the maxima caused by the field reversal are observed. At 1.5 mm only the maxima caused by the hf sheath expansion are visible. Similarly to the experimental results, the maxima observed at 0.4 and 1.5 mm are phase shifted. In the experiment, the spatial resolution is only about 1 mm. Therefore, both mechanisms are observed at the same position in the experiment and are spatially resolved only in the simulation.

Compared with the collisionless single frequency case discussed earlier, excitation at the phase of collapsing sheath is also observed in a dual-frequency discharge in the collisional regime. Due to this analogy the excitation might also be

caused by a local field reversal. Based on previous results in a single frequency discharge in a collisional regime [20], this field reversal might be caused by a collisional drag force on the electrons that prevents electrons from advancing into the sheath. However, electron inertia effects might also contribute [28].

The left plot in figure 11 shows the result of the PIC simulation in terms of a spatio-temporal plot of the electric field under the conditions mentioned above. One can observe the modulation of the sheath electric field with both the high and low frequency. The colour scale is chosen such that brown corresponds to a reversed field at the bottom electrode and dark green to a reversed field at the top electrode (colour online). Except for the phases of field reversal the electric field at the bottom electrode is negative and the electric field at the top electrode is positive.

The right plot in figure 11 shows the indicated area of the left plot enlarged. It shows a spatio-temporal plot of the electric field close to the bottom powered electrode during the first half of one low frequency RF cycle under the same conditions. At phases of collapsing high and low frequency sheath there is a local reversal of the electric field at the sheath edge. A reversed field is indicated by the white colour and is clearly observable in

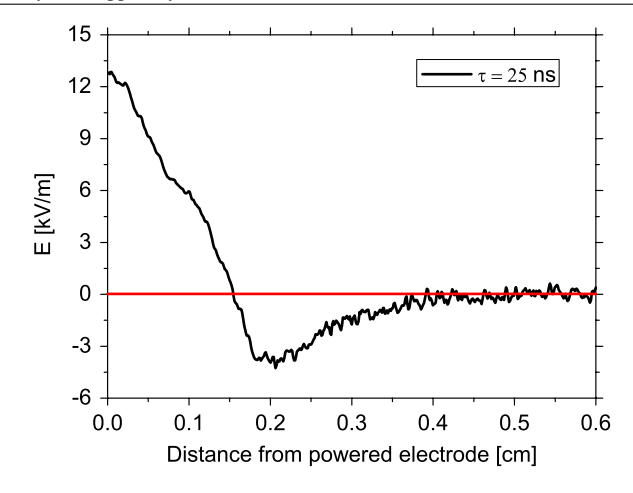


Figure 12. Electric field in dependence on the distance from the bottom powered electrode in a dual-frequency helium discharge operated at 65 Pa at a specific phase of 25 ns (red horizontal line in figure 11) as it results from a PIC simulation.

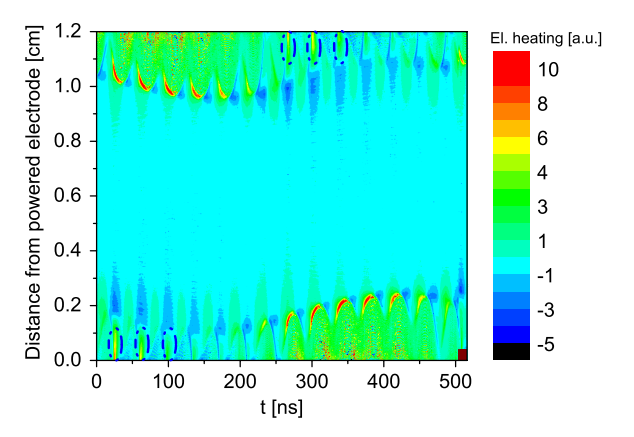


Figure 13. Spatio-temporal plot of the electron heating in a dual-frequency helium discharge operated at 65 Pa as it results from a PIC simulation. Phases when a local field reversal is observed are indicated by circles.

this plot. At the same phases additional excitation is observed (figure 10). Therefore, this excitation seems to be caused by a local field reversal. The same effect is observed at the top electrode during the second half of one low frequency (If) RF cycle, since the discharge is symmetric.

Figure 12 shows a spatial profile of the electric field under these conditions at the specific phase of $\tau=25\,\mathrm{ns}$ (red horizontal line in the right plot of figure 11). At this phase the low and high frequency (hf) sheaths collapse simultaneously. Close to the bottom electrode, the field is positive (field reversal), and close to the sheath edge it shows a minimum (negative field). Towards the bulk it approaches zero. The maximum observed value of the reversed field is about $13\,\mathrm{kV}\,\mathrm{m}^{-1}$.

Figure 13 shows a spatio-temporal plot of the electron heating in the Exelan as it results from a PIC simulation under the same conditions as before. Here the electron heating is defined as dissipated power:

$$p(t) = j(t)E(t), (5)$$

where j is the current density and E the electric field. Red corresponds to heating and blue to cooling (negative heating, colour online). Heating is generally observed at phases of hf sheath expansion, when beams of highly energetic electrons are generated by the expanding sheath. However, positive heating is also observed at phases when hf and lf sheaths collapse simultaneously and a reversed field is observed (circles in figure 13). The deposited power at these phases leads to the experimentally observed excitation at phases of field reversal (see figure 10). The observed positive heating in the sheath at phases of full lf sheath expansion is assumed to be caused by secondary electrons.

Such a field reversal is observed not only in helium dual-frequency discharges but also under different conditions in other gases. Figure 14 shows the space and time-resolved electric field close to the bottom electrode during the first half of one If RF cycle in a dual-frequency argon discharge at 13 Pa as it results from a PIC simulation. The applied frequencies and geometry are the same as before. The applied voltages are $V_{\rm lf}=1000\,{\rm V}$ and $V_{\rm hf}=500\,{\rm V}$. A gas temperature of 500 K, a secondary electron emission coefficient of $\gamma=0.25$ and an electron reflection coefficient of $\alpha=0.2$ are used as input parameters. The white areas in figure 14 correspond to reversed fields again.

Figure 14 also shows a spatial profile of the electric field at $\tau=27\,\mathrm{ns}$ in argon. Again a reversed field at the bottom electrode is observed. The electric field shows a minimum (negative field) close to the sheath edge and approaches zero towards the bulk. The local minimum of the electric field at the sheath edge corresponds to an ambipolar field. As discussed in detail in the following section, the heavy ions cannot follow the collapsing sheath as fast as the electrons. Consequently, an ambipolar field builds up to couple electron and ion motion.

A similar local extremum of the electric field at the position of the maximum sheath width during the phase of sheath collapse is observed in the simulation of a single frequency CCRF discharge modelled by a fluid sheath model [40,41]. Figure 15 shows three spatially resolved electric field profiles close to the powered electrode in a symmetric single frequency argon discharge operated at 13.56 MHz and 10 Pa. The time averaged field (solid black line) and the field at the phase of maximum sheath expansion (dotted blue line) as well as at the phase of minimum sheath expansion (dashed red line) are shown. The simulation was performed in a cylindrical discharge with equal electrode areas of 500 cm² and an inter electrode spacing of 6 cm. An electron temperature of 2.5 eV, a gas temperature of 350 K and a RMS voltage of 190 V were used as input parameters. Absolute values of the electric field are plotted in figure 15 on a logarithmic scale in order to emphasize the local extremum during sheath collapse. All fields are negative under these conditions. No reversed field is observed. However, similarly to the dual-frequency case a local extremum at the maximum sheath width during the sheath collapse, an ambipolar field, is observed. A field reversal due to electron inertia cannot be observed applying this model, since electron inertia is neglected.

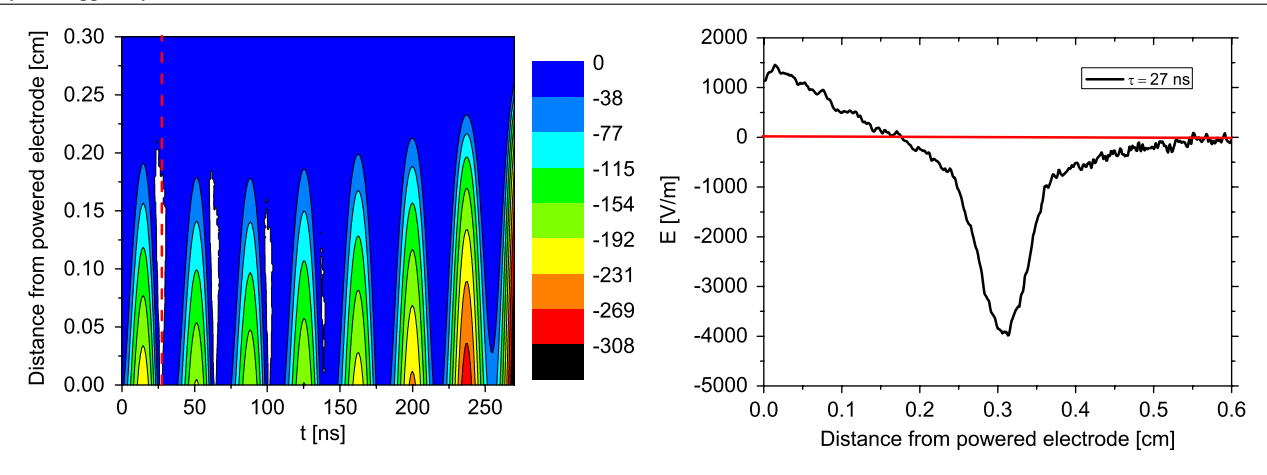


Figure 14. (Left) Spatio-temporal plot of the electric field close to the bottom powered electrode in a dual-frequency argon discharge operated at 13 Pa during the first half of one low frequency RF cycle (PIC simulation). The electric field is given in units of kV m⁻¹. (Right) Electric field in dependence on the distance from the bottom powered electrode at 13 Pa at a specific phase of 27 ns (red dashed line in left graph).

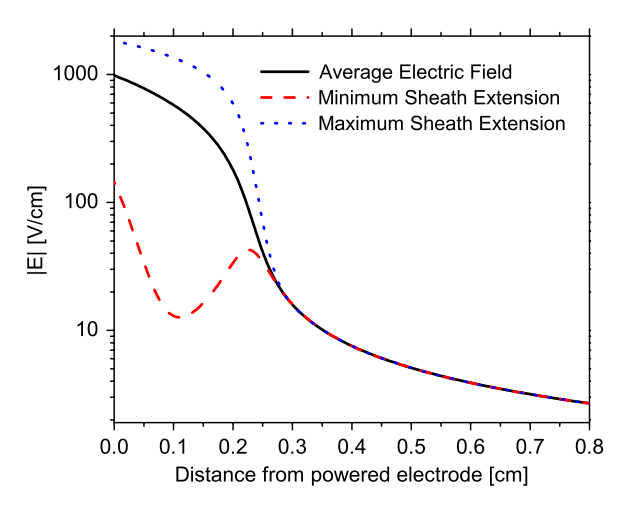


Figure 15. Absolute values of spatially resolved electric fields close to the powered electrode in a single frequency CCRF discharge in argon at 10 Pa calculated using a fluid sheath model [40,41]. The time averaged field (solid black line) and the field at the phase of maximum sheath expansion (dotted blue line) as well as at the phase of minimum sheath expansion (dashed red line) are shown.

5. Discussion

Local reversals of the electric field during sheath collapse are observed in single as well as dual-frequency CCRF discharges. In asymmetric, single frequency discharges, additional excitation during the phase of sheath collapse is observed at low pressures (≤1 Pa) in molecular as well as rare gas discharges. The tilt of the observed maximum in the spatio-temporal plots of the excitation indicates an electric field that accelerates electrons towards the electrode at this phase. In a symmetric dual-frequency discharge, a field reversal is observed both experimentally and theoretically at relatively high pressures of 65 Pa. Based on earlier investigations [14, 19, 20, 22, 28–30] these field reversals can be caused by different mechanisms depending upon the pressure. At low pressure it is caused by electron inertia and at high pressures by electron collisions with the background gas and electron inertia. However, in both cases the effect is the same. Electrons cannot follow the fast collapsing sheath. Consequently, a reversed electric field builds up that accelerates electrons towards the electrode in order to support a constant current.

In this paragraph, a simple fluid model is developed, which describes the field reversal in the different regimes qualitatively. This model is limited to those regions where the condition of quasineutrality is fulfilled and the current dominated by electron conduction current. Displacement current is not included in the model. It does not describe how the sheath is filled with electrons.

The momentum balance equation for electrons in a discharge without magnetic fields is given by

$$mn\left[\frac{\partial \vec{u}}{\partial t} + (\vec{u} \cdot \nabla)\vec{u}\right] = -en\vec{E} - \nabla p - mnv_c\vec{u}$$
 (6)

where m is the electron mass, $n=n_{\rm e}=n_{\rm i}$ the plasma density, \vec{u} the electron velocity, e the elementary charge, \vec{E} the electric field, p the pressure and $v_{\rm c}$ the collision frequency for elastic collisions of electrons with the neutral background gas.

As only the electron motion perpendicular to the electrode (defined as the x direction) is relevant here and only gradients in this direction occur, equation (6) reduces to

$$n\left[\frac{\partial u}{\partial t} + u\frac{\partial u}{\partial x}\right] = -\frac{enE}{m} - \frac{kT_{\rm e}}{m}\frac{\partial n}{\partial x} - n\nu_{\rm c}u \tag{7}$$

with $\nabla p = kT_e \nabla n$. Here u and E are the x-components of \vec{u} and \vec{E} , respectively, k the Boltzmann constant and T_e the electron temperature.

Substituting the current density j = -enu into equation (7) assuming a stationary ion density profile one obtains

$$\frac{\partial j}{\partial t} + j \frac{\partial u}{\partial x} = \frac{e^2 nE}{m} + \frac{ekT_e}{m} \frac{\partial n}{\partial x} - \nu_c j. \tag{8}$$

The continuity equation is given by

$$\frac{\partial n}{\partial t} + \frac{\partial}{\partial x}(nu) = 0. (9)$$

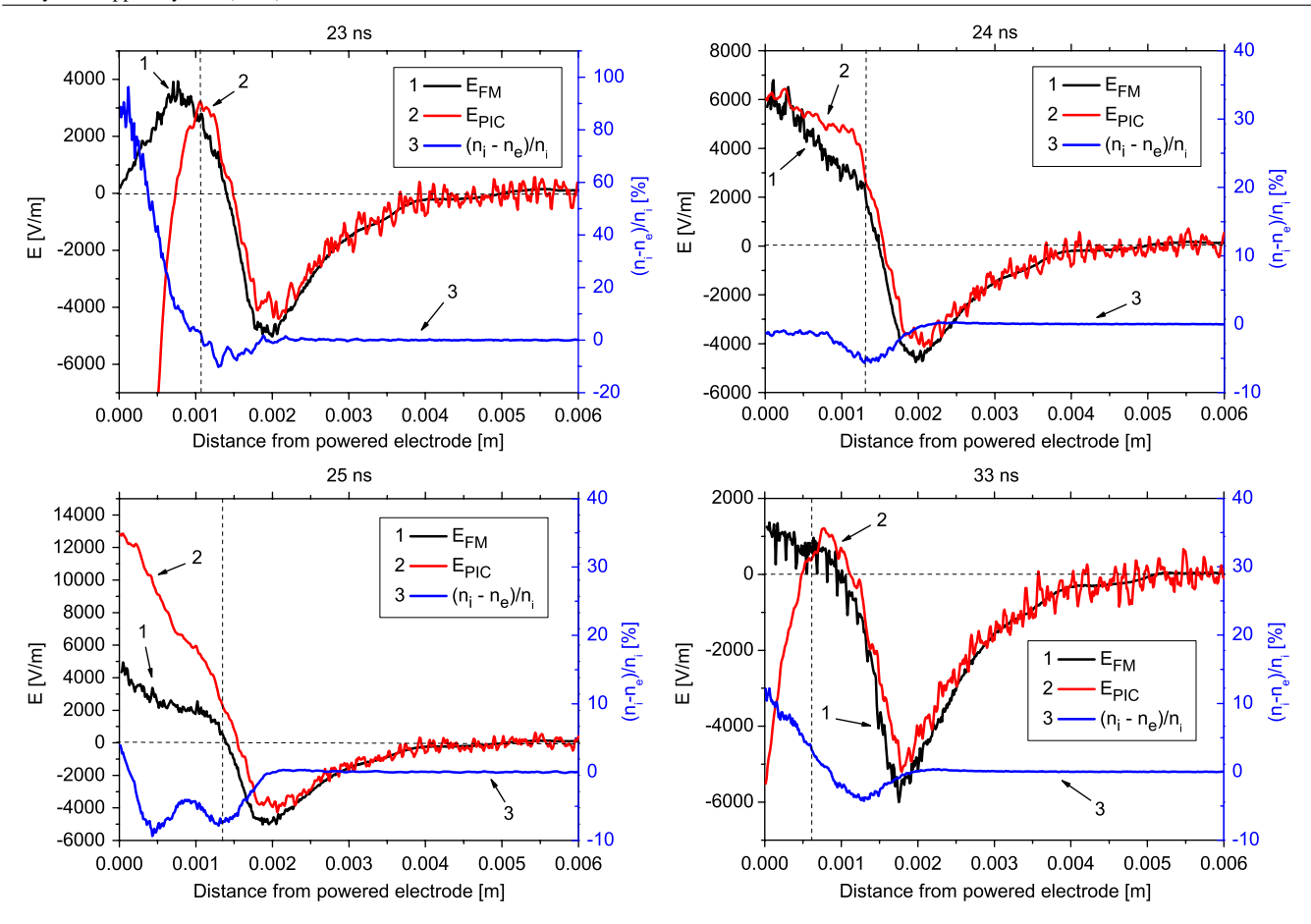


Figure 16. Spatial profiles of the electric field in front of the powered electrode as they result from the fluid model (equation (11), black line 1) and the PIC simulation (red line 2) in a dual-frequency CCRF discharge in helium at 65 Pa at different phases of 23, 24, 25 and 33 ns. The spatial profile of the relative deviation from quasineutrality at each phase is also shown (blue line 3, right scale).

A simple analysis based on the global particle balance shows that the ionization rate in the sheath can be neglected in the continuity equation, if the sheath width is much smaller than the bulk length and the ion density in the sheath is much lower than in the bulk. Further, the excitation during the phase of sheath collapse is more than one order of magnitude smaller than the excitation caused by the hf sheath expansion (see figures 8 and 10). Therefore, ionization is assumed to be dominated by the hf sheath expansion and there is no source term in equation (9), which is used to describe the phase of the field reversal. Secondary electrons could also contribute to ionization. They are not necessarily visible in the observed emission pattern. However, this effect would have no relevance as a source term in the context discussed here. Under the assumption of a stationary density profile $((\partial n/\partial t) = 0)$ equation (9) reduces to

$$\frac{\partial u}{\partial x} = \frac{j}{en^2} \frac{\partial n}{\partial x}.$$
 (10)

Substitution of equation (10) into equation (8) yields the following expression for the electric field at the bulk side of the sheath edge:

$$E = \frac{m}{ne^2} \left(\frac{\partial j}{\partial t} + \nu_c j + (j^2 - j_{th}^2) \frac{1}{en^2} \frac{\partial n}{\partial x} \right)$$
(11)

with $j_{\text{th}}^2 = \frac{e^2 n^2 k T_{\text{e}}}{m}$.

The first and third terms on the RHS of equation (11) correspond to an electric field due to electron inertia. The first term is attributed to temporal changes of the electron current and the third one to the electron velocity and its spatial changes. The second term corresponds to collisions and the fourth one to diffusion.

Applying equation (11) to a given set of input parameters yields a detailed understanding of the cause of an observed field reversal, since different mechanisms can be separated. In the following, this fluid model is applied to a dual-frequency CCRF discharge under conditions that were investigated both experimentally as well as theoretically (see section 2.2). Input parameters in terms of electron current density and ion density profiles as well as collision frequency ($v_c \approx 8 \times 10^8 \, \text{s}^{-1}$) and electron temperature ($T_{\rm e} \approx 2.6\,{\rm eV}$) are all taken from the PIC simulation presented before. Here the case of a He discharge operated at 65 Pa (see section 4) is investigated. Under these conditions a field reversal is observed during different time intervals within one If RF cycle (see figure 11), when If and hf sheaths collapse simultaneously. During these time intervals additional excitation is observed close to the bottom powered electrode (see figure 10). For example, a strong field reversal is observed between 22 and 34 ns. In the following, this time interval is discussed in detail:

Figure 16 shows a comparison between the electric field resulting from the fluid model (equation (11), black line 1)

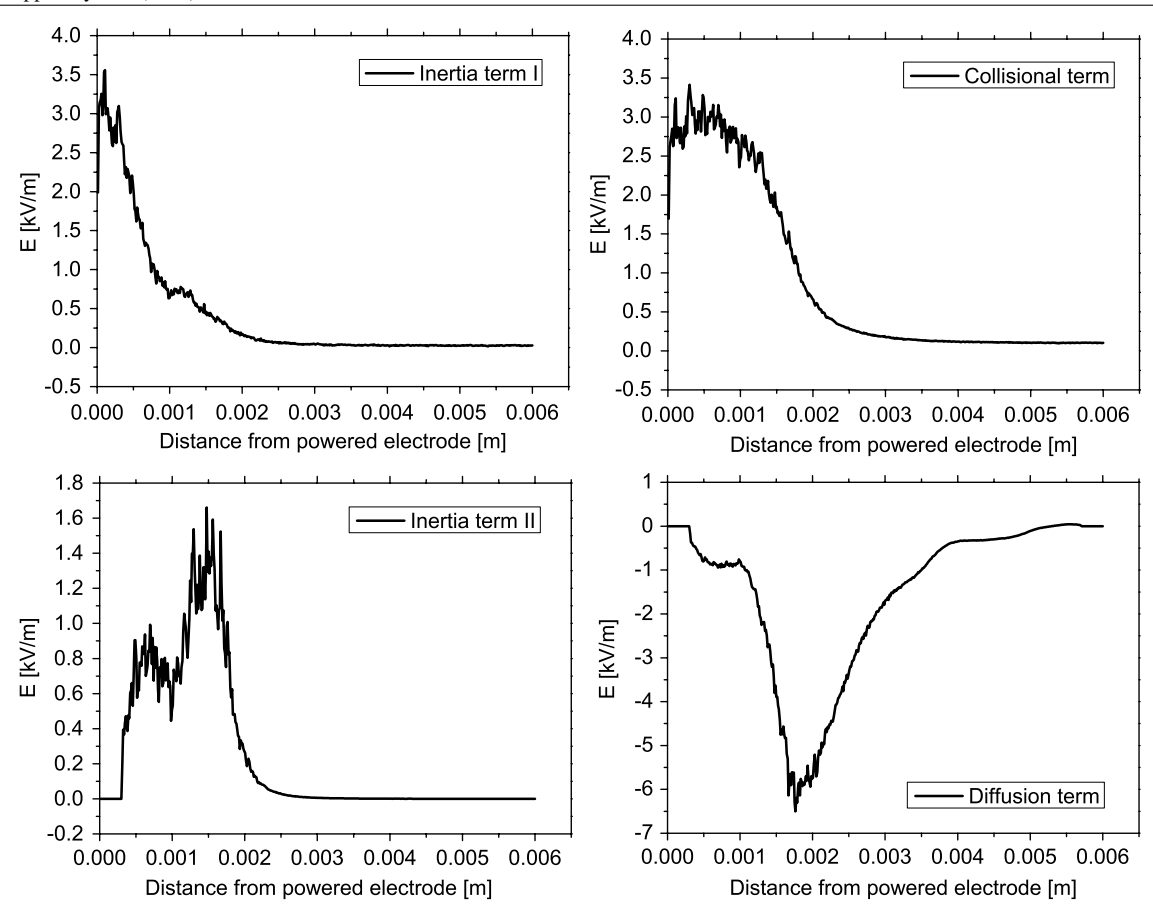


Figure 17. Spatial profiles of the different terms of equation (11), which contribute to the electric field in front of the powered electrode at 24 ns. Inertia term I corresponds to the first term in equation (11), collision term to the second, inertia term II to the third and diffusion term to the fourth.

using input parameters from the PIC simulation and the electric field directly resulting from the PIC simulation (red line 2). It shows spatial profiles of the electric field at different phases within one hf period (23, 24, 25, 33 ns). Good agreement between the fluid model and PIC simulation is found as long as the condition of quasineutrality is fulfilled (blue line 3). At 23 ns the sheath is retreating; however, it is not yet fully collapsed. In the sheath, where quasineutrality is violated, the fluid model is not applicable. As the sheath collapses electrons are transported from the bulk towards the electrode in order to fill up the ion matrix. Since the ion density close to the electrode is lower than in the bulk a higher electric field is needed in the sheath region compared with the bulk region in order to keep a constant current. This field is generated by a local negative charge excess at the sheath edge, which is clearly visible in figure 16 (23 ns).

Figure 16 (24 ns) shows a comparison between electric field profiles obtained from the fluid model (black line 1) and the simulation (red line 2) one nanosecond later. Now the sheath is fully collapsed and the condition of quasineutrality is fulfilled almost everywhere. Only at the sheath edge an excess of negative charges is observed again. High values of the reversed field (6 kV m $^{-1}$) are observed and well reproduced by the fluid model.

Figure 17 shows the respective contributions of the individual terms of equation (11) to the total electric field at

this phase. The black line 1 in figure 16 (24 ns) is the sum of these four terms. The origin of the negative field between the bulk and the sheath edge is clearly electron diffusion. As electrons are much lighter than the He ions, they can follow the collapsing sheath faster by diffusion. The ions cannot follow and the electrons move away from them. This leads to an ambipolar field between the negative charge excess close to the sheath edge and the positive charge excess in the bulk. The amplitude of this ambipolar field is determined by the decay length of the ion density $(1/n_i)(\partial n_i/\partial x)$. The reversed field at 24 ns is caused by both electron inertia and electron collisions with the neutral background gas to similar extents. At the other phases discussed here the relative contributions of the individual terms to the electric field are similar. Obviously, the discharge is operated in a transition regime between the inertially and collisionally dominated regime. Under these conditions both mechanisms contribute equally to the field reversal. At much lower pressures, such as the single frequency case investigated here, the field reversal can only be caused by electron inertia. At much higher pressures collisions are responsible for a field reversal.

One more nanosecond later, at 25 ns, the reversed electric field is even stronger (figure 16 (25 ns)). At this phase an interesting phenomenon is observed: As shown in figure 16 (25 ns) quasineutrality is violated in the vicinity of the electrode and the fluid model is no longer applicable. However,

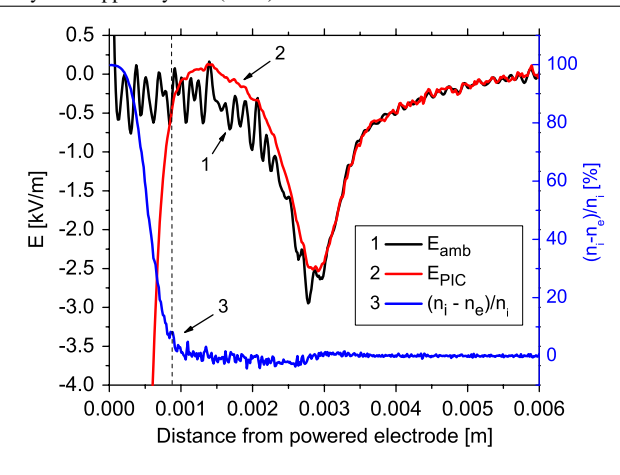


Figure 18. Electric field in dependence on the distance from the bottom powered electrode in a dual-frequency argon discharge operated at 65 Pa at a specific phase of 27 ns as it results from the calculation of an ambipolar field (black line 1) and PIC simulation (red line 2). The relative deviation from quasineutrality is also shown.

there is no conventional sheath consisting of an excess of positive charges. At this phase the electrode charges up positively due to ion bombardment and to compensate the ion current. Consequently, a sheath filled with electrons is observed at this phase. A similar phenomenon was observed by Vender theoretically in a single frequency discharge [29].

At the end of the time interval, when a field reversal is observed, the (ion) sheath expands again. The corresponding electric field profiles at a phase of 33 ns are shown in figure 16 (33 ns). Shortly after this phase, a beam of energetic electrons is generated by the expanding sheath that penetrates into the plasma bulk [9].

In argon, the field reversal is much less pronounced. However, an ambipolar field that couples electron and ion motion is also observed. Figure 18 shows the spatial profile of the electric field in argon close to the powered bottom electrode during the phase of sheath collapse at 27 ns as it results from a PIC simulation (red line 2). In this case the discharge is operated at 65 Pa. The applied frequencies and geometry are the same as before. The applied voltages are $V_{\rm lf} = 500 \, \rm V$ and $V_{\rm hf} = 220 \, \rm V$. A gas temperature of 600 K, a secondary electron emission coefficient of $\gamma = 0.1$ and an electron reflection coefficient of $\alpha = 0$ are used as input parameters. In order to verify the hypothesis that the extremum present in figure 18 is caused by an ambipolar field the field is calculated based on the assumption of an ambipolar field using the ion density profile and electron temperature ($T_e = 1.4 \,\mathrm{eV}$) resulting from the PIC simulation as input parameters. The ambipolar field E_{amb} is given by [1]

$$E_{\rm amb} = \frac{D_{\rm i} - D_{\rm e}}{\mu_{\rm i} + \mu_{\rm e}} \frac{\nabla n_{\rm i}}{n_{\rm i}} \approx -\frac{D_{\rm e}}{\mu_{\rm e}} \frac{\nabla n_{\rm i}}{n_{\rm i}}.$$
 (12)

Here n_i is the ion density taken from the PIC simulation, D_i and D_e the ion and electron diffusion coefficients and μ_i and μ_e the ion and electron mobilities. The electron diffusion coefficient and mobility are generally

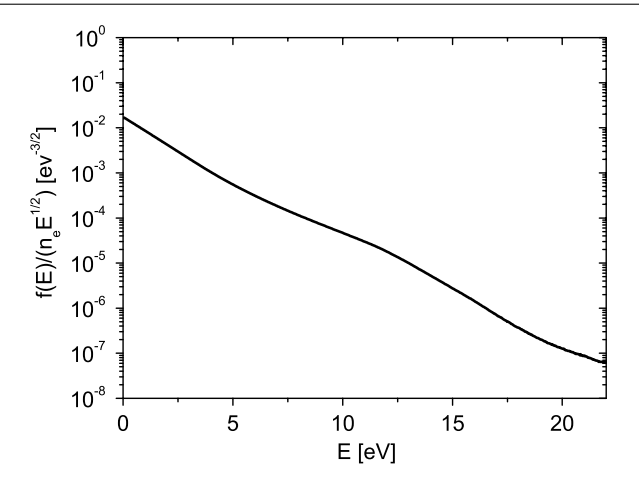


Figure 19. Normalized time averaged electron distribution function in the centre of the discharge as it results from the PIC simulation (argon, 65 Pa)

given by [1]

$$D_{\rm e} = \frac{4\pi}{3n_{\rm e}} \int_0^\infty \frac{v^4}{\nu_{\rm m}(v)} f_{\rm e0} \, \mathrm{d}v, \tag{13}$$

$$\mu_{\rm e} = -\frac{4\pi e}{3mn_{\rm e}} \int_0^\infty \frac{v^3}{v_{\rm m}(v)} \frac{{\rm d}f_{\rm e0}}{{\rm d}v} {\rm d}v. \tag{14}$$

Here $\nu_{\rm m}(v)$ is the effective collision frequency for momentum transfer for electrons and $f_{\rm e0}$ the isotropic part of the electron distribution function $f_{\rm e}$. Generally $\nu_{\rm m}(v)$ depends on velocity and, therefore, the above integrals must be solved explicitly to get $D_{\rm e}$ and $\mu_{\rm e}$.

However, in the case of Maxwellian distribution functions D_e and μ_e are related by the Einstein relation [1]:

$$\frac{D_{\rm e}}{\mu_{\rm e}} = \frac{kT_{\rm e}}{\rm e}.\tag{15}$$

Figure 19 shows the normalized time averaged electron distribution function in the plasma bulk as it results from the PIC simulation under the conditions discussed here. As a good approximation the distribution function is Maxwellian and the Einstein relation is, therefore, used to calculate the ambipolar field (equation (12)).

The result of this calculation is shown in figure 18 (black line 1). As the electric field profile obtained from the simulation is reproduced well, the local extremum of the electric field near the sheath edge can be identified with an ambipolar field. In a single frequency discharge ambipolar fields during the phase of sheath collapse are also observed (figure 15).

In principle this fluid model could also be applied to the single frequency CCRF discharge under the conditions investigated experimentally here. At high pressures a similar model was developed before and applied to a hydrogen discharge [20]. At lower pressures experiments or simulations yielding the input parameters needed for the model might be difficult, but interesting for future investigations. In this context it should be noted that at such low pressures and in asymmetric discharges the current can be non-sinusoidal due to the PSR effect [23, 33, 34, 35].

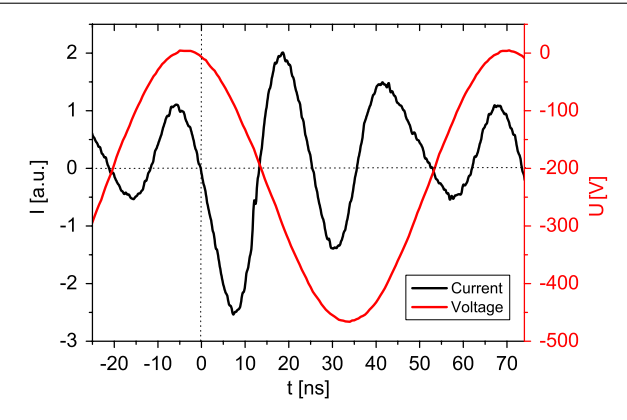


Figure 20. Measured current and voltage in a single frequency, neon discharge operated at 1 Pa and 8 W.

Figure 20 shows phase resolved measurements of the RF current and voltage in neon under the conditions investigated experimentally here. The high frequency oscillations of the RF current at such low pressures are not completely damped until the end of the RF cycle. Due to the PSR effect the spatial oscillation of the sheath within one RF period is non-sinusoidal. It leads to a faster expansion and collapse of the sheath and has, therefore, probably an important influence on the occurrence of a field reversal.

Furthermore, in asymmetric discharges such as the single frequency discharge investigated here there is a dc bias, which is nearly equal to the RF amplitude of the voltage, if the discharge is strongly asymmetric. This dc bias affects the field reversal at the powered electrode, since it leads to bigger sheath widths at the driven electrode. Consequently, the sheath collapses faster in asymmetric than in symmetric discharges at a given RF voltage amplitude and plasma density. With increasing velocity of the collapsing sheath the reversed field needed to keep a constant current also increases. If there is a dc bias the ion density at the powered electrode will decrease. Consequently, the electron density at the powered electrode at the phase of sheath collapse will also be lower. Therefore, a given ion flux to the electrode is compensated less effectively, if there is a dc bias, and a higher reversed field is needed to ensure this compensation. In the case of the dual-frequency discharge investigated here there is almost no dc bias, since to a good approximation the discharge is symmetric. In the experiment the plasma is shielded from the chamber walls by confinement rings. The degree of symmetry was tested by the degree of symmetry of the spatio-temporal excitation profile (see figure 8). Therefore, the assumption of a voltage source that is purely RF in the PIC simulation is justified. If asymmetric discharges are investigated, the simulation will have to be modified in this respect.

6. Conclusions

Field reversals in single and dual-frequency CCRF discharges were investigated experimentally as well as theoretically. In both discharges the maxima of the excitation during phases of sheath collapse are observed by PROES indicating a field reversal.

In an asymmetric single frequency discharge field reversals are observed at low pressures below 1 Pa in rare gases as well as in molecular gas discharges. In a symmetric dual-frequency discharge field reversals are observed at the phases when the high and low frequency sheaths collapse simultaneously. In the dual-frequency case the experimental results in terms of spatio-temporal excitation profiles are compared with the results of a PIC simulation. This simulation explicitly shows reversed fields at distinct phases. A fluid model used to calculate the electric field during sheath collapse is developed. Using input parameters from the simulation the resulting electric field profiles agree well with the field directly obtained from the PIC simulation in regions of quasineutrality, where the model is applicable. Based on this model, different mechanisms leading to the observed field profiles are separated and the physical causes of the field reversal understood.

Depending on the discharge conditions, a field reversal in capacitive discharges can either be caused by electron inertia (low pressures), collisions of electrons with the background gas (high pressures) or a combination of both (intermediate pressures). Each of these mechanisms can prevent electrons from instantaneously following the collapsing sheath. If electrons cannot follow the retreating sheath by diffusion, a reversed field builds up that accelerates electrons towards the electrode in order to keep a constant current and to compensate the ion flux to the electrode within one RF cycle.

It is shown explicitly for the dual-frequency discharge that was investigated experimentally that the field reversal is equally caused by both electron inertia and collisions.

During a time interval of a few nanoseconds the electrode can be charged up positively by ion bombardment at phases of vanishing external voltage. At these phases a sheath of electrons (negative charge excess) is observed in front of the electrode. As the ion density decreases towards the electrode a higher field is needed at the electrode than in the bulk to keep a constant current.

Electron diffusion leads to an ambipolar field at the position of maximum sheath width that couples electron and ion motion. It is caused by the fact that electrons can follow the collapsing sheath faster than the heavy ions. Such ambipolar fields are observed in PIC simulations of dual-frequency discharges in different gases and in calculations of the electric field in a single frequency argon discharge using a fluid sheath model.

In general, field reversals are observed in both single and dual-frequency CCRF discharges. As electrons gain additional energy through the reversed fields, field reversals contribute significantly to plasma heating. A detailed understanding of the underlying mechanisms might be relevant for industrial processes, since it contributes to plasma production and can lead to charged surfaces.

Acknowledgments

This work has been funded by the DFG through SFB 591 and GRK 1051, the Hungarian Scientific Research Fund through grants OTKA-T-48389 and OTKA-IN-69892 and supported by Andor Technology. The dual-frequency measurements

were performed in collaboration with Timo Gans, Deborah O'Connell, Bert Ellingboe and Miles Turner and supported by Lam Research Inc., the EU (FP5), the DFG (SFB 591 and GRK 1051) and the Studienstiftung des dt. Volkes.

References

- [1] Lieberman M A and Lichtenberg A J 2005 *Principles of Plasma Discharges and Materials Processing* 2nd edn (New York: Wiley-Interscience)
- [2] Boyle P C, Ellingboe A R and Turner M M 2004 Plasma Sources Sci. Technol. 13 493–503
- [3] Boyle P C, Ellingboe A R and Turner M M 2004 J. Phys. D: Appl. Phys. 37 697
- [4] Kitajima T, Takeo Y, Petrovic Z L and Makabe T 2000 Appl. Phys. Lett. 77 489
- [5] Denda T, Miyoshi Y, Komukai Y, Goto T, Petrovic Z L and Makabe T 2004 J. Appl. Phys. 95 870
- [6] Kawamura E, Lieberman M A and Lichtenberg A J 2006 Phys. Plasmas 13 053506
- [7] Turner M M and Chabert P 2006 Phys. Rev. Lett. 96 205001
- [8] Gans T, Schulze J, O'Connell D, Czarnetzki U, Faulkner R, Ellingboe A R and Turner M M 2006 Appl. Phys. Lett. 89 261502
- [9] Schulze J, Gans T, O'Connell D, Czarnetzki U, Ellingboe A R and Turner M M 2007 J. Phys. D: Appl. Phys. 40 7008–18
- [10] Lieberman M A and Godyak V A 1998 IEEE Trans. Plasma Sci. 26 955
- [11] Surendra M and Graves D B 1991 Phys. Rev. Lett. 66 1469
- [12] Turner M M 1995 Phys. Rev. Lett. 75 1312
- [13] Gozadinos G, Turner M M and Vender D 1995 Phys. Rev. Lett. 87 135004
- [14] Salabas A, Marques L, Jolly J and Alves L L 2004 J. Appl. Phys. 95 4605–20
- [15] Vender D and Boswell R W 1990 *IEEE Trans. Plasma Sci.*
- [16] Wood B P 1991 PhD Thesis University of California at Berkely
- [17] Tochikubo F, Suzuki A, Kakuta S, Terazono Y and Makabe T 1990 J. Appl. Phys. 68 5532
- [18] Petrović Z Lj, Tochikubo F, Kakuta S and Makabe T 1992 J. Appl. Phys. 71 2143
- [19] Leroy O L, Stratil P, Perrin J, Jolly J and Bellenguer Ph 1995 J. Phys. D: Appl. Phys. 28 500
- [20] Czarnetzki U, Luggenhölscher D and Döbele H F 1999 Plasma Sources Sci. Technol. 8 230–48
- [21] Gans T, Schulz-von der Gathen V and Döbele H F 2004 Europhys. Lett. 66 232–8
- [22] Mahony C M O, Wazzan R Al and Graham W G 1997 Appl. Phys. Lett. 71 608–10

- [23] Schulze J, Heil B G, Luggenhölscher D, Czarnetzki U and Brinkmann R P 2008 J. Phys. D: Appl. Phys. 41 042003
- [24] Schulze J, Kampschulte T, Luggenhölscher D and Czarnetzki U 2007 J. Phys. Conf. Ser. 86 012010
- [25] Salabas A and Brinkmann R P 2005 Plasma Sources Sci. Technol. 14 S53–9
- [26] Godyak V A, Piejak R B and Alexandrovich B M 1992 Plasma Sources. Sci. Technol. 1 36
- [27] Belenguer Ph and Boeuf J P 1990 Phys. Rev. A 41 4447
- [28] Sato A H and Lieberman M A 1990 J. Appl. Phys. 68 6117
- [29] Vender D and Boswell R W 1992 J. Vac. Sci. Technol. A 10 1331
- [30] Turner M M and Hopkins M B 1992 *Phys. Rev. Lett.* **69** 3511
- [31] Tochikubo F, Makabe T, Kakuta S and Suzuki A 1993 J. Appl. Phys. 73 2163
- [32] Gottscho R A 1987 Phys. Rev. A 36 2233
- [33] Mussenbrock T and Brinkmann R P 2006 Appl. Phys. Lett. 88 151503
- [34] Mussenbrock T and Brinkmann R P 2007 Plasma Sources. Sci. Technol. 16 377–85
- [35] Czarnetzki U, Mussenbrock T and Brinkmann R P 2006 Phys. Plasmas 13 123503
- [36] Miller P A, Hebner G A, Greenberg K E, Pochan P D and Aragon B 1995 J. Res. Natl Inst. Stand. Technol. 100 427
- [37] NIST Atomic Spectra Database http://physlab.nist.gov/cgi-bin/AtData/main_asd
- [38] Klick M 1996 J. Appl. Phys. 79 3445
- [39] Klick M, Kammeyer M, Rehak W, Kasper W, Awakowicz P and Franz G 1998 Surf. Coat. Technol. 98 1395
- [40] Kratzer M, Brinkmann R P, Sabisch W and Schmidt H 2001 J. Appl. Phys. 90 2169
- [41] Brinkmann R P 2007 J. Appl. Phys. 102 093302
- [42] Mussenbrock T, Hemke T, Ziegler D, Brinkmann R P and Klick M 2008 Plasma Sources Sci. Technol. 17 025018
- [43] Donkó Z and Petrović Z Lj 2006 Japan. J. Appl. Phys. 45 8151
- [44] Morgan W L, Boeuf J P and Pitchford L C The Siglo Data base, CPAT and Kinema Software http://www.siglo-kinema.com
- [45] Phelps A V and Petrović Z Lj 1999 Plasma Sources Sci. Technol. 8 R21
- [46] Phelps A V 1994 J. Appl. Phys. 76 747
- [47] Phelps A V http://jilawww.colorado.edu/avp/collisiondata/ unpublished
- [48] Turner M M 2006 Phys. Plasmas 13 033506
- [49] Turner M M, Chabert P, Levif P, Boyle P and Robiche J 2007 Proc. 18th Int. Conf. on ICPIG (Prague, Czech Republic, 15–20 July 2007) G08
- [50] Böhm C and Perrin J 1992 Rev. Sci. Instrum. 64 31-44
- [51] Schulze J, Heil B, Luggenhölscher D, Czarnetzki U and Ellingboe A R 2007 *Bull. Am. Phys. Soc.* **52** 4